Modeling impact on aluminium sandwich including velocity effects in honeycomb core

Amélie Kolopp, Raquel Alvarado, Samuel Rivallant, Christophe Bouvet

To cite this version:

Amélie Kolopp, Raquel Alvarado, Samuel Rivallant, Christophe Bouvet. Modeling impact on aluminium sandwich including velocity effects in honeycomb core. Journal of Sandwich Structures and Materials, 2013, 13 (6), pp.733-757. 10.1177/1099636213501102 . hal-01853146

HAL Id: hal-01853146
https://hal.science/hal-01853146v1

Submitted on 2 Aug 2018

To link to this article: DOI: 10.1177/1099636213501102
URL: http://dx.doi.org/10.1177/1099636213501102

To cite this version: Kolopp, Amélie and Alvarado, Raquel and Rivallant, Samuel and Bouvet, Christophe *Modeling impact on aluminium sandwich including velocity effects in honeycomb core.* (2013) Journal of Sandwich Structures and Materials. ISSN 1099-6362

Modeling impact on aluminium sandwich including velocity effects in honeycomb core

Amélie Kolopp, Raquel A Alvarado,
Samuel Rivallant and Christophe Bouvet

Abstract
A numerical model has been developed on metallic sandwich structures as an armor for aeronautical applications. Several combinations of AA5086-H111 aluminium skins and aluminium honeycomb core have been studied, considering medium-velocity and high-energy impacts. The aim is to establish links between the sandwich performances and the material and geometrical parameters. An elasto-plastic, strain-rate dependent behavior has been implemented to represent the skins and the core. The sandwich model has been calibrated and validated from the experimental data. Dynamic effects, as well as strong couplings between the skins and the core appear to have a significant effect on the target performance.

Keywords
Impact, metallic sandwich, aluminium honeycomb, experiments, modeling

Introduction

Metallic sandwich structures are typically assembled with steel or aluminium thin skins and a metallic lightweight core such as honeycomb or foam. They appear to be potential armor architectures, providing a good bending rigidity without a significant increase in structural weight. Therefore, they are currently used for instance as protective solution for the rear bulkhead of planes or against underwater shocks in naval applications [1,2]. These structures are also foreseen as a

---

Université de Toulouse, INSA, UPS, Mines Albi, ISAE, ICA (Institut Clément Ader) ISAE (Institut Supérieur de l'Aéronautique et de l'Espace), Toulouse Cedex, France

Corresponding author:
Christophe Bouvet, ISAE / ICA, 8 av. Edouard Belin, Toulouse 31000, France.
Email: christophe.bouvet@isae.fr

potential evolution of the aircraft fuselage [3], combining the usual requirements (aerodynamics, conductivity, EMI, etc.) with a protection against foreign object impacts (ice or engine debris for instance).

In this paper, we focus on the impact behavior of metallic sandwich structures composed of AA5086-H111 aluminium skins and aluminium honeycomb core. We consider medium-velocity and high energy normal impacts with a hard spherical projectile (120 m/s, 1 kJ). This paper follows on from a previous experimental and numerical impact study of AA5086-H111 aluminium plates alone [4]. The aim of this paper is to characterize the behavior of the core and to associate its properties with the sandwich impact performances. Thus, the study is conducted with the given experimental conditions and skin configurations. We consider the results of the aluminium skins alone as a reference case. This approach is original as the skins are mainly studied in sandwich structures and no particular selection criteria are proposed to choose a core and to improve its behavior. Moreover, a first analysis of skins-core couplings is proposed in this study.

A numerical model of aluminium honeycomb has been developed. A multi-scale approach has been chosen to link the local behavior of the cells in compression and the global behavior of the honeycomb in the sandwich. The results showed that strain rate effects in the core compression influence significantly the sandwich behavior and they have been considered in the model to correctly fit the experiments.

Several numerical and experimental impact studies on sandwich structures are available in the literature. Amongst these, only a few deal with the comparison of skins alone and sandwich structures. Goldsmith et al. [5] evaluated the impact performance of AA5052 aluminium plates (0.79 mm for each skin) and of sandwiches with the same skins. Two 19.5 mm thick cores have been tested: hexagonal cell honeycomb ¼-5052-0.002 and Flexcore honeycomb 5052/F40-0.0019 (Hexcel®). The ballistic limit of the skins alone, the sandwich with hexagonal and Flexcore cell reached respectively 108, 56 and 128 m/s. The authors underline that the skins play a major role in the target resistance and energy absorption. However, the core properties seem also to influence the ballistic limit. In the same way, Buitrago et al. [6] conducted impact tests and numerical simulations on sandwiches with composite facesheets and on separated skins alone (carbon fiber with epoxy resin, 2 mm thick). The core is 20-mm thick aluminium honeycomb. In the range of 92–548 m/s, the skins were identified as the main factor responsible for the energy absorption: 46%, 41% and 13% for the front, the rear skin and the core respectively. More globally, Abrate [7] noted that for sandwiches with composite skins, the penetration resistance is mostly governed by the facing resistance and the overall rigidity of the structure. In addition, several studies on underwater shocks on metallic plates and sandwich panels underlined that the back deflection of the skins alone is higher than for sandwiches [1,2].

Regarding the numerical modeling of honeycomb, two main approaches can be found in the literature. Several authors consider the real geometry of the honeycomb cell in the sandwich structures [1,2,6]. To simplify the modeling, others represent the honeycomb by the behavior of a unit vertical edge [8–10], mostly in low-velocity impact applications. Aminanda et al. studied the crushing mechanisms of several honeycombs using different cell walls (Nomex, aluminium, and paper). They showed that the load–displacement is mostly driven by the vertical edges, and they represent the honeycomb as grid of non-linear springs. This representation showed a good correlation with the experiments. Asadi et al. [10] modeled the aluminium honeycomb by a vertical edge stabilized by three branches with symmetry conditions. This model fitted the experiments considering elasto-plastic behavior of the walls without strain rate sensibility. However, several authors investigated the strain rate effects on cellular materials crushing behavior [11–14] for shock and armor applications. It appears that dynamic effects can be noticed over a strain rate threshold, which depends on the tested structure. Under this limit, the behavior is closed to the quasi-static, which can be attributed to the negligible change in the material behavior or by micro-inertial effects [11,12]. Radford et al. [13] and Elnasri [14] studied the dynamic effects occurring in the metallic honeycomb during compression. Radford conducted compression tests varying the initial velocity (using Hopkinson bars with 50 m/s of initial velocity). The experiments showed a significant load increase with the impact velocity. The authors attributed this tendency to several possible mechanisms: strain rate effects in the wall materials, dynamic buckling behavior (higher buckling modes activated in dynamic compression) and propagation of a plastic wave before the onset of buckling.

The experimental impact set-up, target description and impact results of sandwich targets are given in section ‘‘Experimental impact tests’’. Then, the honeycomb modeling is described in section ‘‘Sandwich model description’’. The numerical results of aluminium sandwich panels subjected to impacts are compared with the experiments and an analysis is addressed in section ‘‘Numerical results and model validation’’. In the final section, concluding remarks are given.

Experimental impact tests

Experimental set-up

Impact tests have been conducted using a gas gun. In this paper, we focus on normal and centered impacts of rigid projectiles (see Figure 1). A rigid spherical projectile of 30 mm diameter and of 127 g is launched at an average velocity of 120 m/s. The tested sandwich configurations are square targets of 200 to 400 mm side. The targets are simply supported at the rear by a square rigid frame of 170 mm side, regardless of the sample size. This boundary condition has been chosen to be more representative of a real structure (600 mm side panels) compared to clamping along four edges, and to simplify the associated numerical model. Note that in the present application, the tested armors are considered as non-structural protections, which are placed before the working structure with a 50 mm gap. Therefore, a back deflection of the target inferior to this gap is allowed. In this paper, we define the

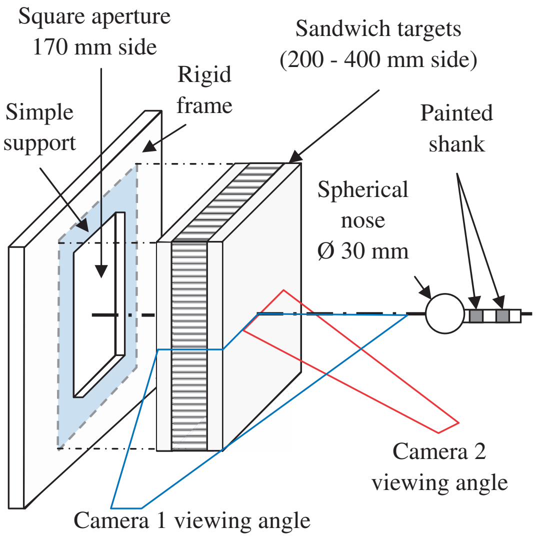

Figure 1. Impact test set-up: boundary conditions and instrumentation.

critical speed as the velocity for which the target partially fails without reaching the structure perforation (rupture of the front or the rear skin only for example).

During the impact test, the projectile position is measured with a high-speed camera (camera 1 in Figure 1) located perpendicularly to the trajectory. A second camera is also used to obtain qualitative data on the front skin damage during the impact. The recording frame of the camera is set to 75 pictures/ms. This value is a compromise between the available picture size (256 × 64 pixels) and the number of measuring points (from 30 to 75 points during the projectile velocity decrease). The measurement errors are mainly attributed to the picture blur and differences in lighting. However, they remain inferior to ±5 m/s in the measure of initial and residual velocity. A post-processing program is used to detect the projectile during the impact (thanks to the painted shank at the rear of the spherical nose) and to calculate the instantaneous velocity. The impact duration typically comprised between 0.4 and 1 ms, depending on the tested case (target perforation or projectile rebound).

The damage and deformation of sandwich samples are observed after impact. Both skins are painted following a speckle pattern and their deformed shapes are measured by 3D digital image correlation using Vic3D software. The horizontal line through the maximum indentation point (impact location) is averaged to obtain a one-quarter profile as shown in Figure 4.

Sandwich targets description

Sandwich targets have been assembled using two AA5086-H111 aluminium sheets as front and rear skins (1 or 2 mm thick). The core is 20 mm thick aluminium comb with hexagonal cells as described in Figure 7(b) (reference ACG-3/8, m^3). The skins and the core are assembled using an adhesive film (Redux® 0, 300 g/m^2).

previous impact study was conducted on AA5086-H111 aluminium plates under the same conditions [4]. The results showed that two 2 mm thick of 200 mm side were not perforated. However, a critical speed of 122.6 m/s en observed for another configuration composed by respectively 2 and 1 mm front and rear skin of 400 mm side. After the impact, only the rear skin failed, gh the front skin remained undamaged.

s study aims to evaluate the core influence by studying comparable sandwich kins configurations. Therefore, two sandwich configurations have been bled and studied, based on the skin impact results (see Table 1):

oup A: targets of 200 mm side (reference case A_{ref}). The sandwich structures assembled using 2 mm thick AA5086-H111 aluminium plates. Two similar gets have been tested and are identified as A_1 and A_2 in this paper.

oup B: targets of 300 mm side. The sandwich structures are assembled using m thick AA5086-H11 aluminium plate as front skin and 1 mm thick plate as r skin. One sandwich has been tested and is identified as B_1. The associated rence case B_{ref} is 400 mm side as it has been shown in [4] that the results are influenced by boundary effects from 300 mm side.

imental results and analysis

t test results are given in Table 1. Thicknesses and rupture indicators asso- with the front and the rear skins are given by t_F/t_R and R_F/R_R. The rupture tors are associated with "Y" in case of rupture and "N" otherwise. The sion L corresponds to the target size. The absorbed energy E_{abs} is the differ- etween the initial kinetic energy E_{ini} (calculated from the initial velocity V_{ini}) e residual energy (calculated from the residual velocity V_{res}). Note that V_{res} gative values in case of projectile rebound and positive values if the target

Table 1. Impact samples and test results.

ID/scheme	L [mm]	t_F/t_R [mm]	V_{ini} [m/s]	E_{ini} [J]	V_{res} [m/s]	E_{abs} [J]/% E_{ini}	R_F/R_R	t_i [ms]	I_{max} [mm]
A_{ref}	200	2/2	126.2	1018	−9.3	1011/99.3	N/N	0.92	31.6
A_1	200	2/2	122.5	953	−6.3	949/99.5	Y/N	0.79	24.2
A_2	200	2/2	125.3	996	24.0	955/95.9	Y/Y	0.89	/
B_{ref}	400	2/1	122.6	954	−21.5	925/96.9	N/Y	0.76	30.6
B_1	300	2/1	117.9	883	62.2	638/72.2	Y/Y	0.59	/

is perforated. The impact duration t_i represents the duration from the beginning of the projectile-target contact until the end of the contact in case of projectile rebound or target perforation. The indentation I_{max} is defined as the maximal out-of-plane displacement of the back skin after impact (taking the support as the reference). Note that this value is not defined in case of target perforation.

Note that the two similar cases A_1 and A_2 differ due to the experimental dispersion on initial velocities (respectively at 122.5 and 125.3 m/s for A_1 and A_2). The critical speed of metallic sandwich structures reaches 122.5 m/s, as the A_1 configuration partially failed without perforation (rupture of the front skin only, as shown in Figure 2(a) and (b)). However, the same sandwich impacted at a slightly higher impact velocity A_2 is totally perforated (Figure 2(c)). The study of these two cases will be useful to calibrate the numerical model that will be constructed afterwards, since two different results have been found for two velocities that are very close to each other.

Several damage mechanisms can be identified from the sandwich samples observation after impact (Figure 2). Case A_1 shows a circular rupture zone of 16 mm

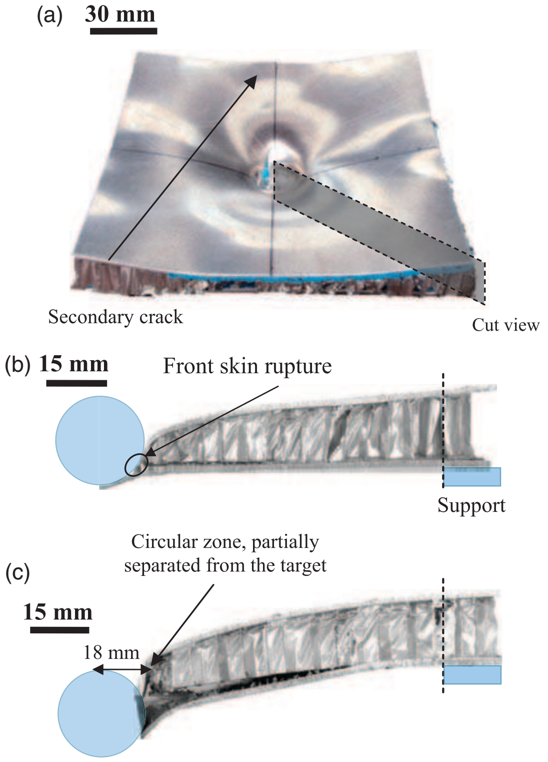

Figure 2. A_1 target: (a) front view; (b) side view, 45° cut and (c) A_2 target, side view, 45°.

diameter on the front skin. Secondary cracks propagate from the initial rupture which leads to a petal rupture shape (see Figure 2(a)). This shape is typically associated with the damage modes of ductile metallic plates [15]. In comparison, the sandwich A_2 is completely perforated and a central circular part of 18 mm radius is detached from the rest of the skin (Figure 2(c)). In both cases, we can notice high deformations of the honeycomb in the impact vicinity, mainly deformed in out-of-plane compression (local crushing) and shear. In addition, the honeycomb is torn near the interface between the core and the rear skin near the impact location (seen in Figures 2(b) and(c) and 3). The remaining upper part of the core is highly crushed and gathers near the front skin failure.

One-quarter deformation profiles after impact can be seen in Figure 4 for A_1 and A_{ref} cases. The upper curve represents the front of the first skin, and the lower one is the back of the rear skin. Note that the rupture of the front skin in the A_1 sample, visible in Figure 2(b) is indicated by a dotted line in Figure 4. The reference case is significantly more indented than the sandwich (+30% than the sandwich case). However, this gap has to be nuanced considering the dispersion in initial velocities (126.2 and 122.5 m/s, respectively).

These results show that the core presence tends to modify the critical zones in the skins, from the rear skins for plates alone to the front skin in sandwich configurations. At the same time, it decreases significantly target resistance against

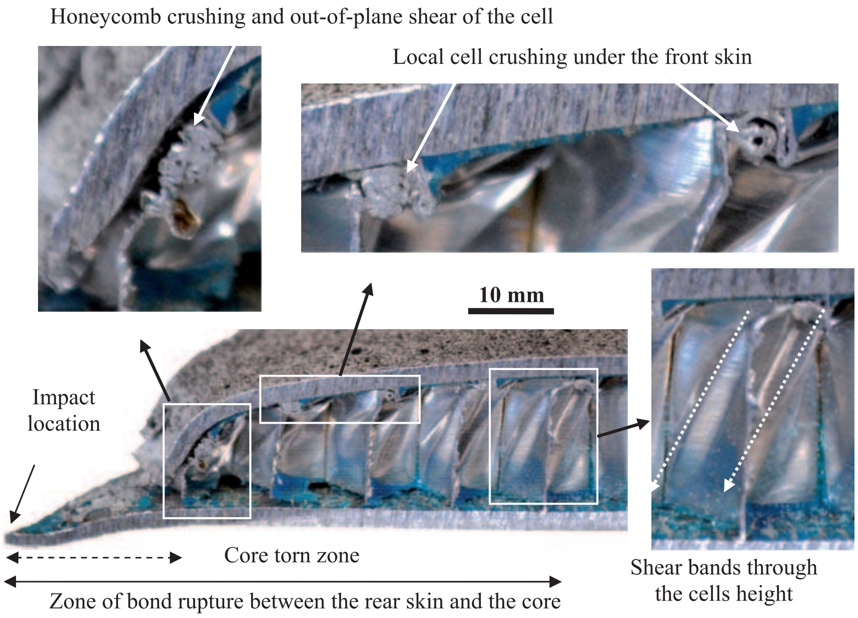

Figure 3. Zoom of the A1 profile after impact: location of honeycomb crushing and shear bands.

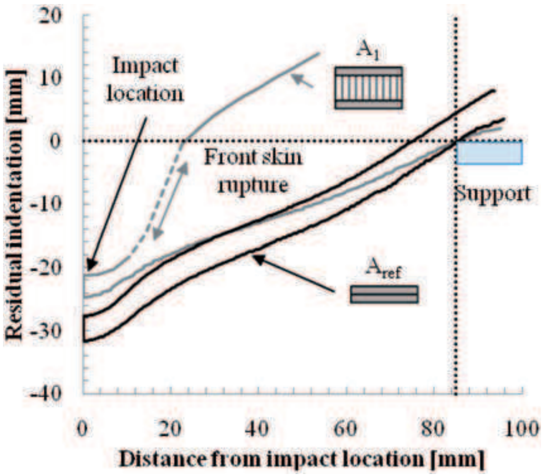

Figure 4. Residual profiles of A_1 and A_{ref} cases.

perforation and the energy absorbed by the target (see Table 1). In return, the residual indentation of sandwich structures is reduced compared to plates alone. The experimental data available are not sufficient to elaborate impact scenario which could explain these differences. However, a possible interpretation can be advanced, considering that the core presence can lead to skins decoupled reactions due to the initial gap between them. The decoupling can be partial or total depending on the core thickness and properties (Figure 5(b) and (c)). This phenomenon is susceptible to initiate premature rupture of the front skin (Figure 5(c)) and thus a significant decrease in the total energy absorbed by the structure, compared to plates alone (Figure 5(a)). However, this hypothesis can be evaluated through numerical impact analysis.

In order to understand the low impact resistance of the sandwich targets (in comparison with the skins alone) and to identify the main mechanisms occurring during the impact (possible de-coupling effects, etc.), a numerical model of aluminium sandwich has been implemented. The model description and results are given in the next sections.

Sandwich model description

The aluminium sandwich model has been built taking into account the tested configurations and the boundary conditions described in the previous section. The numerical simulations are carried out using the commercial finite element software ABAQUS 6.9-2/Explicit. The material model applied to the AA5086-H111 plates will be taken from a previous study [4]. Therefore, we focus in this paper on the modeling of the honeycomb.

In order to validate the numerical results, the following points will be studied: rupture prediction (presence of failed elements, location and rupture shape),

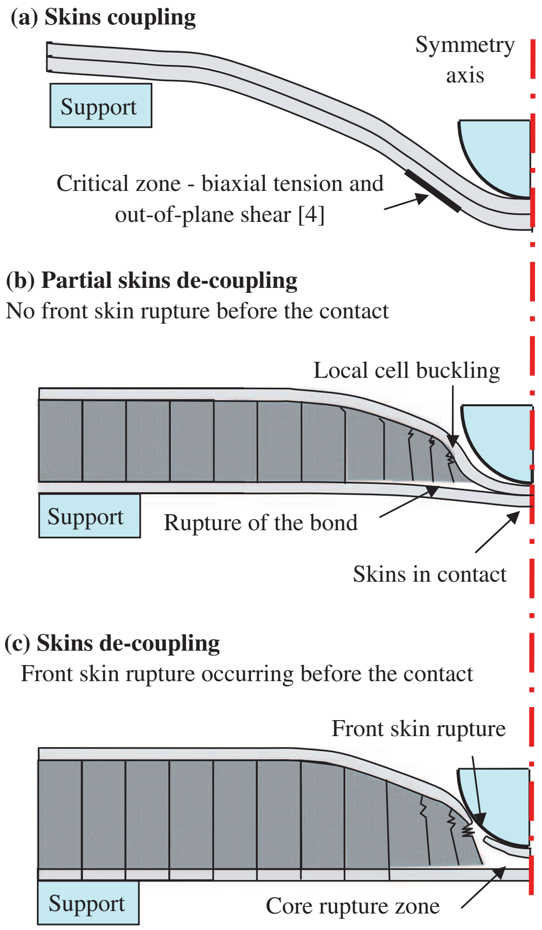

Figure 5. Identification of possible impact scenario in sandwich structures: (a) skins alone; (b) partial decoupling; (c) total decoupling.

evolution of the projectile velocity and displacement and deformed target profiles after impact.

Skins modeling

The material constitutive law of the AA5086-H111 plates has been implemented in a user-defined subroutine VUMAT. Simplified flow stress (equation (1)) and rupture models (equation (2)) based on the Johnson-Cook formulation have been used (justifications in [4]).

$$\sigma = A + Bp^n \tag{1}$$

Table 2. Material parameters used in the AA5086-H111 aluminium plates model.

A (MPa)	B (MPa)	n	$\varepsilon^f_{1/3}$	T	V
143	562	0.6	0.299	−0.483	0.086

$$\varepsilon^f = \varepsilon^f_{1/3} \exp^{T\left(\sigma^* - \frac{1}{3}\right)} (1 + \dot{p})^V \tag{2}$$

The flow stress σ depends on the equivalent plastic strain p and on material parameters A, B and n. In the rupture model, the rupture strain ε^f is calculated taken into account the triaxiality ratio σ^* (mean hydrostatic stress divided by the von Mises equivalent stress) and the strain rate sensibility effects. In the equation (2), $\dot{p}$ is the plastic strain rate and the parameters V, T and $\varepsilon^f_{1/3}$ (rupture strain in quasi-static loading) depend on the material properties. The parameter values used in this study (calibration conducted in [4]) are synthesized in Table 2.

Material failure is represented by the element deletion, which is controlled through the failure criterion F defined below [4]:

$$F = \int_0^t \frac{\mathrm{d}\overline{\varepsilon_P}}{\varepsilon^f} \mathrm{d}t \tag{3}$$

The quantity $\mathrm{d}\overline{\varepsilon_P}$ represents the increment of equivalent plastic strain and ε^f is the rupture strain calculated from equation (2). The failure criterion represents the accumulation of plastic strain in the element and is comprised between zero and one (element deletion).

Geometry, mesh and boundary conditions of the sandwich model

Due to the core orthotropic behavior, the numerical problem can be reduced to 1/4th of the real structure, with corresponding symmetry conditions (Figure 6). Analytic surfaces are defined in order to model the rigid frame acting as a simple support at the rear of the sandwich. The impactor is modeled as a spherical rigid analytic surface of 30 mm diameter (see justification in [4]) representing the fourth of the weight of the real projectile. An initial velocity is imposed (the same as the experimental measure).

Note that the contacts between the structure and the rigid surfaces are frictionless and allow the separation of the two components. As for the bond between the skins and core, a perfect bond condition is imposed (node tie condition).

As far as the mesh is concerned, linear brick elements with reduced integration are used in the plates and the core. The skin mesh is subdivided into four subregions, being more refined at the impact zone. In-plane mesh dimensions are comprised between approximately 0.2 mm side near the impact location and

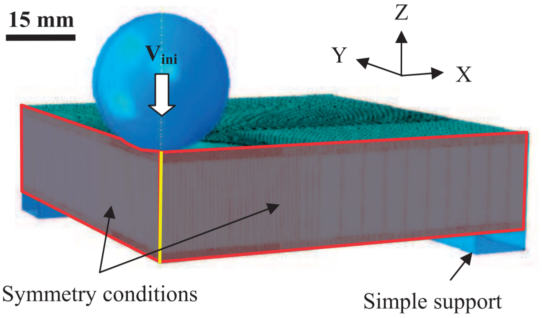

Figure 6. Geometric model of aluminium sandwich and boundary conditions.

3 mm side near the edges. Eight elements per millimeter are used along the thickness direction of the plate (justification in [4]).

In the plane direction, the core mesh does not need the same refinement, since the deformation is governed by the plates during the impact. One element per thickness is used for the honeycomb mesh (see justification in Section "From Mesoscopic to Macroscopic Scale"). This meshing choice has been proved to correctly estimate the effects observed during experimental tests.

As an indication, the impact model of 200 mm side sandwich has about 70,000 elements and needs about 21 CPU hours to model an impact of 1 ms duration. The model of 300 mm side target considered 170,000 elements and needs about 34 CPU hours in the same conditions.

Honeycomb modeling

The honeycomb material properties have been implemented on the model using a VUMAT subroutine on ABAQUS/Explicit. The out-of-plane compression behavior will be described apart in the next section due to its complexity. The following hypotheses are considered for the honeycomb behavior in the other directions:

1. Couplings: shear and compression behaviors appear to be interdependent when considering multi-axial loading of the honeycomb. There is a competition between out-of-plane crushing (compression mode) and cell rotation (shear mode) [16]. In the sandwich, the most strongly affected zone is located at the vicinity of impact. However, when the rupture of the adhesive bond occurs in this zone (Figure 2(b) and (c)), the shear mode disappears. Therefore, the shear and compressive coupling behavior of honeycomb is neglected and each direction is considered separately.
2. Out-of-plane traction behavior: supposed linear elastic and brittle to represent the adhesive film behavior and to consider the potential rupture of the bond between the skins and core. The law parameters are defined from quasi-static tests and are synthesized in Table 3.

Table 3. Mechanical properties of aluminium honeycomb used in the material model.

Compression		Out-of-plane shear				In-plane
E_z (GPa)	σ_z (MPa)	G_{xz} (GPa)	σ_{xz} (MPa)	G_{yz} (GPa)	σ_{yz} (MPa)	E_x, E_y,G_{xy} (GPa)
0.6	1.28	0.28	1.45	0.14	0.9	0.001

3. Transverse shear behavior: perfect plastic law hypothesis. The values of stress plateau σ_{xz} and σ_{yz} as well as the corresponding shear moduli are taken from the constructor data sheet [17]. A limit value of out-of-plane strain has been defined to initiate the element deletion in the model. This criterion aims to take into account the skins-core bond rupture and the local honeycomb rupture shown in the experiments (see Figures 2(b) and (c) and 3).

5

4. In-plane behavior: supposed elastic linear and negligible considering the other directions (low arbitrary values chosen).

The material values used in the model are shown in Table 3.

Honeycomb characterization in quasi-static compression. The out-of-plane quasi-static compression behavior is characterized by three successive phases [18,19] described in Figure 7(a): initial stage of elastic deformation until a peak limit is reached, followed by a "plateau value" of the stress corresponding to the buckling and crushing of the cell wall; the third step is the densification phase characterized by an increase of the compression stress.

Compression tests have been carried out with sandwich structures (aluminium honeycomb and skins) of 100 mm squared side, (which is representative of the honeycomb behavior in terms of number of cells). The presence of skins is necessary to stabilize the sample during the compression and to recreate the correct boundary conditions on the honeycomb–skins interface. The compression speed reaches 3 mm/min (see Figure 7).

Force and displacement captors are used to plot the true stress–strain curve, and the three phases described in Figure 7(a) can be identified in Figure 7(b). This behavior has been modeled with the analytical expression (3), where p is the cumulated out-of-plane plastic strain.

$$\sigma = \frac{C_1}{\cosh(\alpha_1 p)} + \sigma_0 + C_2(e^{\alpha_2 p} - 1) \tag{4}$$

Each term in equation (4) describes one of the three stages of the out-of-plane compression behavior of honeycomb. The first term corresponds to the peak value and the strain decrease. The stress plateau is represented by a constant σ_0. The last term represents the densification phase. Both experimental and analytical curves

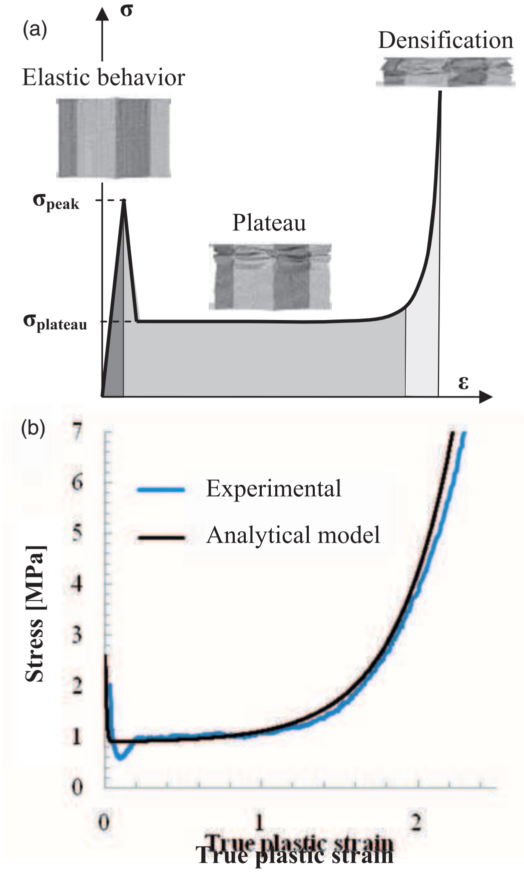

Figure 7. (a) Theoretical compression curve and (b) Experimental and analytical curves in quasi-static compression.

are shown in Figure 6 after the identification of the five parameters of the analytical model $C_1, \alpha_1, \sigma_0, C_2, \alpha_2$.

Numerical results and discussions. A first model of honeycomb sandwich has been built, considering the hypotheses and values given in the previous section. The A_1 and A_2 sandwich cases have been considered (see section "Sandwich Targets Description") and compared to experimental results. The simulations did not fit the experimental results, particularly in terms of rupture prediction. Indeed, in the A_1 case, only the front skin failed, and the target A_2 was totally perforated, whereas the model predicted no skin rupture in both cases.

The strain rate effects occurring during the honeycomb compression have been identified as a potential explanation of these experimental and numerical discrepancies. Indeed, several studies in the literature underline dynamic effects in honeycomb compression behavior [14,13]. The authors observe a significant increase of the peak and plateau stress when increasing the strain rate over a threshold value (depending on the core). This increase can reach more than 20% of the quasi-static value [14]. This effect can be attributed to the propagation of a plastic shock wave [14], and/or material strain rate effects, and/or modification of the buckling modes of honeycomb during compression [13]. However, the origin of this dynamic effect is not still completely understood and validated because of lack of experimental tests that validate the given hypotheses.

In order to evaluate the influence of dynamic effects occurring in the core on the sandwich impact behavior, the strain rate effects are further studied. For this, a numerical model of honeycomb has been built at a mesoscopic scale, i.e. at the scale of a single honeycomb cell. This cell has been subjected to compression under several velocities. This intermediate study will be used to characterize the dynamic honeycomb behavior up to 120 m/s.

Honeycomb mesomodel with strain rate effects

Mesomodel description. The unit cell of the honeycomb considered is an assembly of 3003 aluminium wall. The mesomodel takes into consideration the plastic flow and the strain rate sensitivity of this alloy. A Cowper-Sydmonds model has been chosen to model aluminium wall (see equation (5)).

$$\sigma = \left(A + B\varepsilon^{p^n}\right)\left(1 + \frac{\dot{\varepsilon}^p}{D}\right)^{\frac{1}{q}} \tag{5}$$

The material parameters A, B, n (quasi-static behavior), D and q (dynamic contribution) have been taken from [20] (study on strain rate effects on the flow stress of 3003 grade in tensile tests): respective values of 150 MPa, 62.5 MPa, 1, 30 and 3.5.

The cell geometry and boundary conditions are shown in Figure 8. The cell dimensions are measured from the samples and an average value is indicated in Figure 8(b). Note that the cells are not exactly hexagonal-shaped as the angles between the double wall and single wall reach 130° instead of 120°. In the numerical model, the entire cell is created by rotating one unit branch. The modeling of only one unitary branch is enough to reproduce correctly the quasi-static compression behavior of honeycomb [10]. Nevertheless, the symmetry conditions imposed to construct the complete cell influence the buckling behavior and the strain–stress curves present significant oscillations when only one unit branch is modeled. Therefore, we focus on the behavior of a complete cell in this paper.

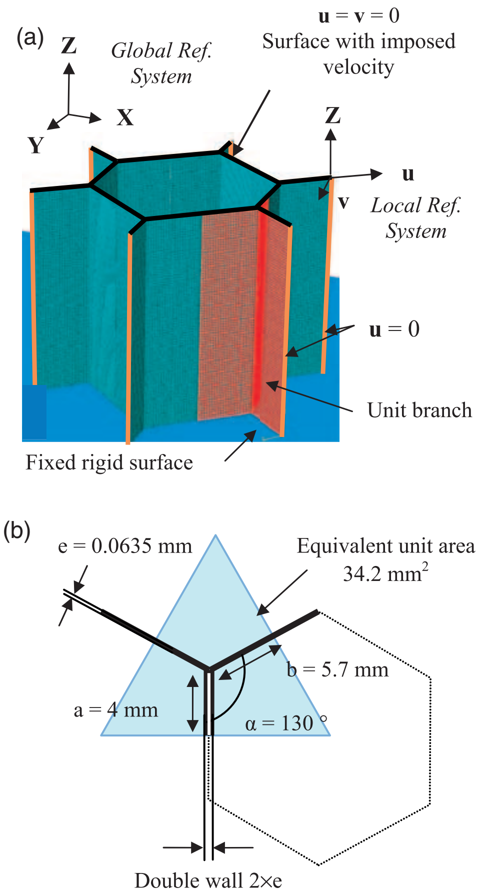

Figure 8. (a) Geometry and boundary conditions of mesoscopic model and (b) Cell geometry.

The double wall in the ribbon direction is taken into account in the model, without considering the influence of the glue. Plate elements are used considering a sufficient mesh refinement to represent the buckling modes and the local crushing observed in reality (square elements of around 0.25 mm side). The unit cell is situated between an upper rigid surface with an imposed velocity and a lower rigid fixed surface. Several compression velocities are tested: 0.12, 1.2, 60 and 120 m/s.

Mesoscopic model results. Figure 9 gives several views of the unit cell for a given upper rigid surface displacement (1.8, 5 and 10 mm). Two velocity cases are considered: 12 and 120 m/s. The cumulative plastic strain is plotted with a filter so as to differentiate the elastic (zero value) and the plastic zones. The 12 m/s case shows plastic zones and onset of local crushing localized in the upper part of the cell,

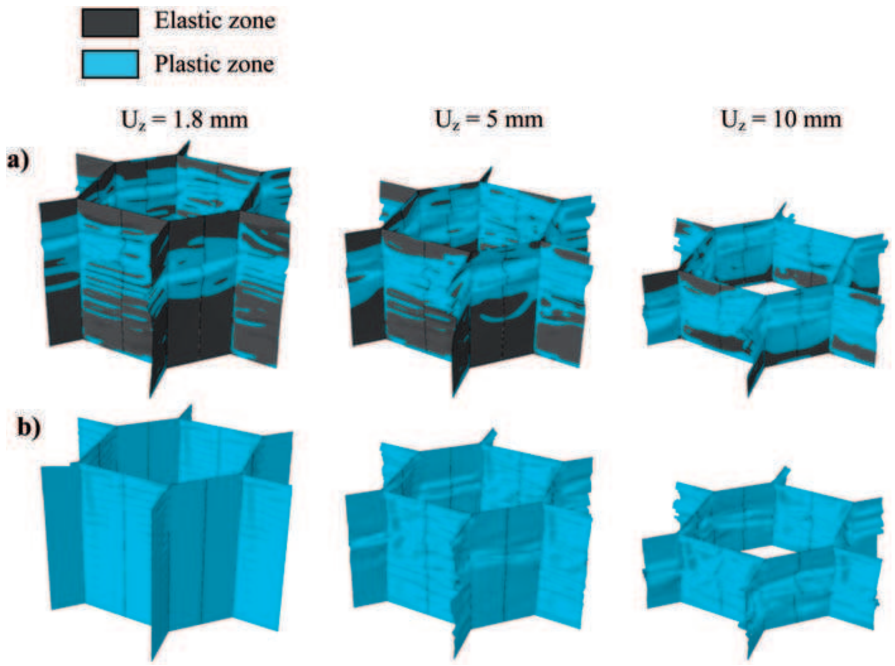

Figure 9. Views of a unit honeycomb cell during compression: (a) 12 m/s and (b) 120 m/s.

while the lower zone remains elastic (Figure 9(a)). On the contrary, for higher velocities (from 60 m/s but clearly visible at 120 m/s), the whole wall height reaches the plastic zone before the onset of buckling (Figure 9(b)). It is also observed that higher order buckling modes are activated at 120 m/s, as mentioned in [13].

The literature evokes three different mechanisms potentially driven by the strain rate:

- *Plastic wave propagation*: aluminium honeycomb reaches plastic domain by means of a plastic wave through thickness prior to the appearance of buckling [14].
- *Material strain rate sensitivity*: stress flow of the aluminium increases with strain rate.
- *Structure effect*: modification of buckling modes with the compression velocity

The stress–strain curves obtained from the cell compression at different velocities are given in Figure 10(b). Both quasi-static experimental and analytical curves are added from Figure 7(b) as reference. No significant velocity effect is observed below 12 m/s in Figure 10(b). However, from 60 m/s, an important increase of the peak and plateau value is visible, without modifying significantly the global

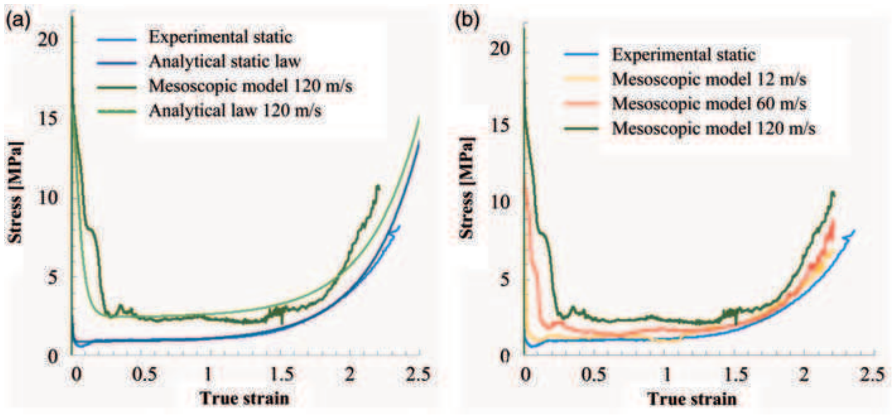

Figure 10. Stress-strain curves obtained from honeycomb compression: (a) Experimental and analytical curves; (b) Experimental quasi-static and numerical curves for several velocities.

Table 4. Stress values and volume energy dissipated in a cell for several velocities.

Compression velocity [m/s]	1.2	12	60	120
Peak value [MPa]	6.7	8	14.4	21.6
Plateau value [MPa]	0.9	0.9	1.7	2.5
Compression energy per volume of a unit cell [mJ/mm^3]	7.3	8.1	13.5	22.6

evolution of the curve (the three steps of the compression remain visible). The stress peak and plateau values are synthesized in Table 4.

A fit of the numerical curves given in Figure 10(b) can be obtained by identifying a set of parameters which depends of the compression velocity. As only the peak and plateau values evolve with the compression velocity, the corresponding parameters C_1, α_1, σ_0 are renamed with an asterisk to indicate their evolution with the velocity v_i. The theoretical law obtained is presented in equations (6) and (7). The fit of the numerical result obtained for 120 m/s is given as example in Figure 10(a).

$$\sigma = \frac{C_1^*}{\cosh(\alpha_1^* p)} + \sigma_0^* + C_2(e^{\alpha_2 p} - 1) \tag{6}$$

$$\begin{cases} \sigma_0^* = 0.008 \times v_i^{1.1} + 0.9 \\ C_1^* = \frac{v_i^{0.8}}{4} + 1.7 \\ \alpha_1^* = \frac{1}{0.006 \times v_i + 0.013} \end{cases} \tag{7}$$

An estimation of the energy dissipated in the cell can be calculated from the curves of Figure 10(b). The energy has been calculated taking into account the peak phase (elastic deformation of the cell and collapse of the wall) and until $\varepsilon = -2$ for all the honeycomb cells. This energy per volume of a honeycomb cell is shown in Table 4. The energy absorbed in a unit cell is significantly higher when increasing the velocity (factor of 3 between quasi-static value and 120 m/s). This indicates that the honeycomb performance (energy per unit weight) is improving with the compression velocity, which is a priori not consistent with the low performance of sandwich structures compared to plates alone. Thus, further investigations, particularly at the macroscopic scale, have to be conducted.

From mesoscopic to macroscopic scale. The mesoscopic model depends on the compression velocity of the core through the parameters σ_0^*, C_1^*, et α_1^* in equation (6). This velocity is approximated by an equivalent macroscopic velocity (defined in equation (8)), which depends naturally on the initial core height h_0.

$$v_i = e^{\varepsilon_z} \times \dot{\varepsilon}_z \times h_0 \tag{8}$$

The ε_z and $\dot{\varepsilon}_z$ parameters represent respectively the strain and strain rate in the Z direction. The definition of a characteristic length (h_0 in this model) is often used in gradient-dependent constitutive models [21–23]. It allows defining a mesh-size independent modeling in the macroscopic model. Therefore, a unique element can be defined through the core thickness (Figures 6 and 13), which represents an average in the thickness of the cells compression behavior. This approach allows the element deletion along the entire core height, which represents correctly the rupture of the skins-core adhesive bond observed experimentally (Figure 13).

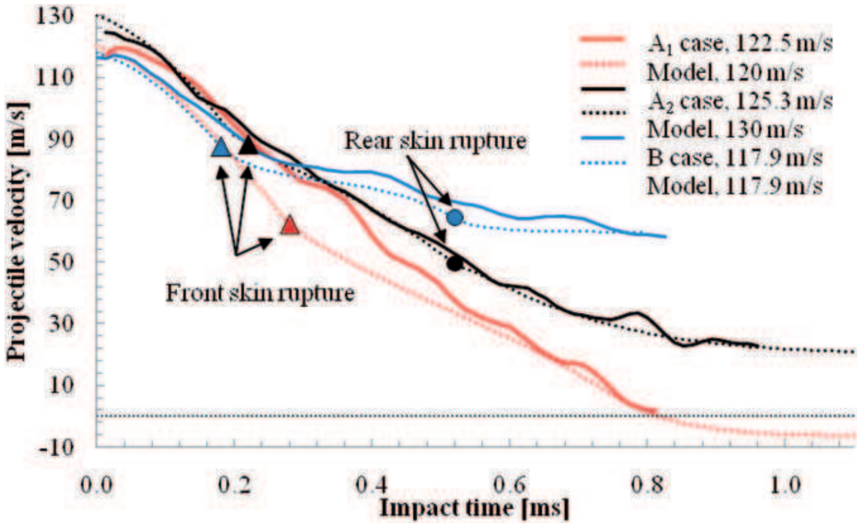

Figure 11. Velocity evolution of experimental cases and associated numerical models.

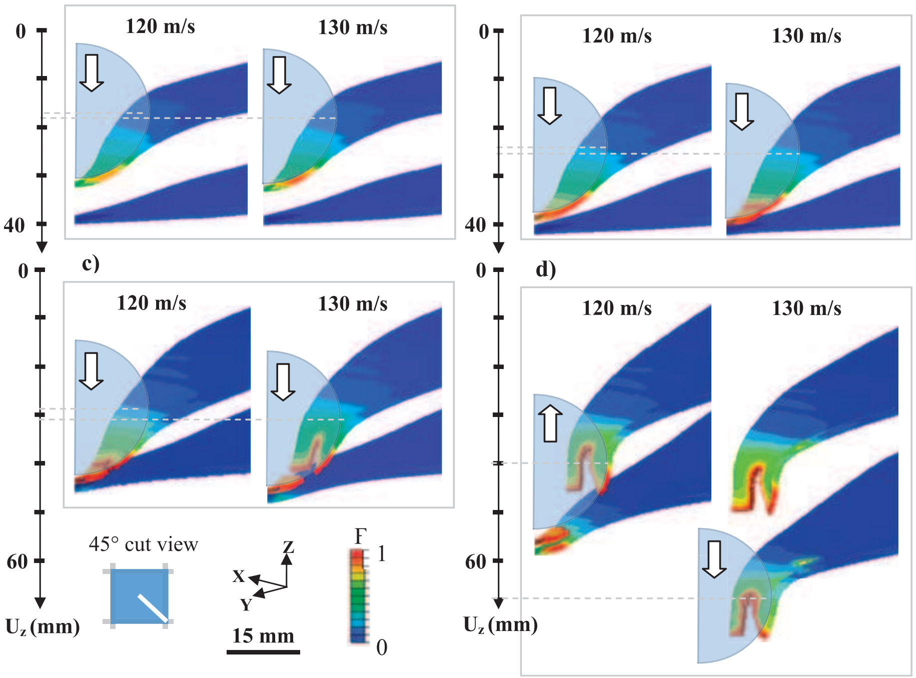

Figure 12. Mapping of the rupture criterion F in the skins for A_1 targets impacted respectively at 120 and 130 m/s; Projectile displacement after: (a) 0.15 ms; (b) 0.23 ms; (c) 0.3 ms and (d) 1.5 ms.

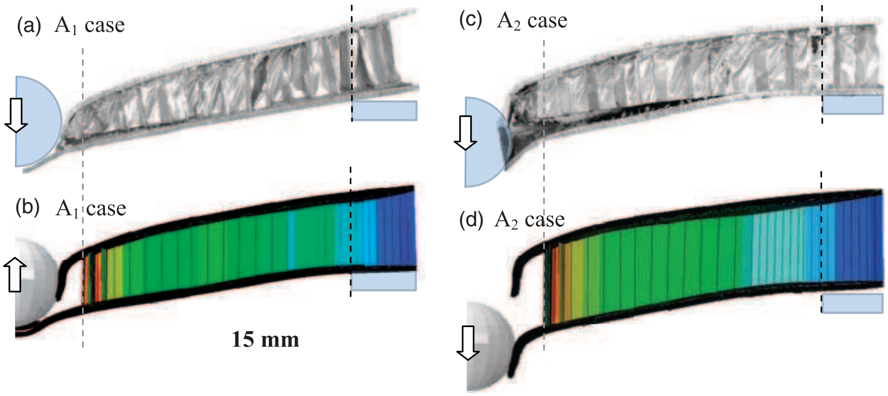

Figure 13. A_1 profiles: (a) Experiment at 122.5 m/s; (b) Model after 1.5 ms at 120 m/s; A_2 profiles: (c) Experiment at 125.3 m/s and (d) Model after 1.5 ms at 127 m/s.

Table 5. Experimental and model results of impact test on aluminium sandwich.

ID/scheme	V_{ini} [m/s]	E_{ini} [J]	R_F/R_R	V_{res} [m/s]	E_{abs}/% E_{ini} [J]	I_{max} [mm]	
Case A_1	Experiments	122.5	953	Y/N	−6.3	949/99.5	24.2
	Model results	122.5	953	Y/Y	−7.8	946/99.3	–
		120	914	Y/N	−10.3	911/99.6	18.2
Case A_2	Experiments	125.3	996	Y/Y	24.0	955/95.9	–
	Model results	125.3	996	Y/Y	−6.9	701/70.4	–
		127	1024	Y/Y	2.8	1023/100	–
		130	1073	Y/Y	21.0	1045/97	–
Case B_1	Experiments	117.9	883	Y/Y	62.2	638/72.2	–
	Model results	117.9	883	Y/Y	59.6	657/74.4	–

Note that the sandwich geometry, mesh, and boundary conditions are the same than those described in section “Geometry, mesh and boundary conditions of the sandwich model”.

Numerical results and model validation

The numerical results of sandwich structures are synthesized in Table 5. The experimental data described in Section “Experimental impact tests” are reminded as comparison. Several points are studied to validate the model: rupture prediction and projectile velocity evolution, residual target profiles and energy absorbed in the structure.

Rupture prediction and projectile velocity evolution

These two points are directly linked and are thus treated together (see Table 5 and Figure 11). It can be seen in Table 5 that numerical results at 122.5 and 125.3 m/s do not fit the corresponding experimental cases. Indeed, in the A_1 case, the model predicts the target rupture whereas only the first skin is perforated in the reality. However, the residual velocity values are close (−6.3 and −7.8 m/s respectively for the measure and the model). In the A_2 case, the model predicts correctly the target rupture, but the residual velocities differ significantly (24 and −6.9 m/s respectively for the measure and the model). Note also that the numerical cases tested at 122.5 and 125.3 m/s show quite similar results. They predict the onset of rupture of both skins without reaching the target perforation (projectile rebound). A circular cap is formed under the projectile and detached from the rest of the skins ($I_{\max}$ not given for these cases). This implies that the model prediction is not accurate enough to foresee the transition from partial to total rupture observed experimentally. It may be due to modeling hypotheses (rupture by element deletion does not take into account the real failure propagation, necking is not considered in the material law, the numerical damage is symmetric due to the representation of a quarter of the target, etc.) or to experimental inaccuracies. However, a good correlation can be observed between the experimental A_1 results and the numerical case at 120 m/s. In the same way, the model at 130 m/s correctly fits the experimental A_2 case tested at 125.3 m/s. Thus, a confidence interval can be defined from ±4% of initial velocity (or ±8% in initial kinetic energy) where the rupture and residual velocity predictions are close to the experimental results.

The projectile velocity curves from experiments and simulations are compared in Figure 11. They are useful to identify impact stages and the onset of rupture. Markers are added to indicate the onset of rupture of the skins according to the numerical simulations.

Three main steps can be identified [4]. A sharp drop in the projectile velocity can be observed in both experimental and numerical curves. This is associated with a local indentation of the front skin and the core. Note that this step remains quite similar in all the tested cases, until approximately 0.2 ms impact duration. Then a slope transition occurs as the projectile deceleration decreases. It is typically associated with a global move of the target with structure bending in skin configurations [4]. In sandwich structures, this mechanism is coupled with the front skin rupture which decreases the target resistance. Note that the curves differ from this point, probably because of the discrepancies in the onset of rupture for each case. Thus, a slight delay in the onset of rupture is likely to influence significantly the target perforation and the velocity evolution. This point is also illustrated in Figure 12. The third step corresponds to the end of impact, characterized by a constant velocity value (positive if the target is perforated and negative in case of projectile rebound).

As noticed previously, the experimental case A_1 (122.5 m/s) correctly fits the simulation at 120 m/s. In the same way, the case A2 (125.3 m/s) is close to the simulation at 130 m/s. The model predicts the front skin rupture from 0.22 ms impact duration at 130 m/s. The rupture is delayed in the model at 120 m/s as the rupture appears from 0.28 ms impact duration. Note also that the case B_1 (300 mm side target) shows a good correlation between the experimental results and the model for the same initial velocity. The three-step curves are clearly marked by two inflexion points which represent successively the rupture of the front and the rear skin.

Several numerical views of 120 and 130 m/s cases are added in Figures 12 and 13 to complete the analysis. Figure 12 gives a local mapping of the rupture criterion near the impact point. The front and back skins are represented without the core to simplify the visualization. Note that for each skin, the front and rear faces are visible to visualize accurately the critical zones location.

The discrepancies in the onset of rupture at 120 and 130 m/s are illustrated in Figure 12(b). Indeed, the front skin rupture occurs before the skins contact at 130 m/s. This can be identified as a total decoupling case, as represented in Figure 5(c). On the contrary, the A_1 case at 120 m/s corresponds to the partial decoupling case described in Figure 5(b) (see Figure 11(c)), as the front skin rupture appears after the contact. Note that the formation of a circular rupture at the rear of the front skin propagates through the thickness to the front face. In a second step, secondary cracks occur and petals are formed under the projectile as shown in the targets after impact. However, the real rupture shapes cannot be represented by the model due to the imposed model symmetries.

Residual target profile

The numerical and experimental deformed shapes are given in Figure 13. The rupture of respectively the front skin and both skins can be observed for cases A_1 and A_2. It is initiated first in the front skin, where a rupture crown is formed and the center is separated from the rest of the skin. Then, if the projectile has enough kinetic energy, the rupture is transmitted to the back skin. The honeycomb cells located under the projectile are compressed and removed from the impact zone. In the model, this effect is well represented by the element deletion condition in shear.

Energy absorption repartition

The energy of the global model is divided into several parts: elastic, plastic, kinetic, artificial, and viscosity. The kinetic energy is maximal at the onset of impact and decreases with the projectile braking. At the same time, the contributions of the elastic and plastic dissipation increase. The energies absorbed through viscosity and artificial effects (meshing stabilization to avoid element distortion) are checked to ensure that these contributions remain negligible in comparison with the total energy of the model.

The repartition of energy absorption is useful to understand the role of each part of the sandwich. This repartition is given in Table 6 for the front skin, the core and the rear skin in several cases. The energy is mainly absorbed through plasticity. The remaining kinetic energy E_{res} corresponds to the kinetic energy of the target and the projectile at the end of the calculation (the calculation is stopped at the beginning of the projectile rebound for time saving reasons). This residual energy is negligible compared to the initial kinetic energy of the projectile: between 0.2% and 4% for sandwich at 120 and 130 m/s, respectively.

The dissipated energy repartitions are compared in Table 6 for sandwich structures impacted at 120 and 130 m/s and for the reference case A_{ref} (values from [4]).

Table 6. Numerical energy repartition for A targets and the associated reference case.

ID/scheme	V_{ini} [m/s]	E_{ini} [J]	R_F/R_R	E_{front} [J]/% E_{ini}	E_{core} [J]/% E_{ini}	E_{back} [J]/% E_{ini}	E_{res} [J]/% E_{ini}
A_{ref}	126.2	1011	N/N	493.5/49	–	494/49	23/2
A_{num}	120	914	Y/N	439/48	271/30	202/22	2.2/0.2
	130	1073	Y/Y	422/39	270/25	342/32	40/4

The sandwich impacted at 120 m/s shows roughly the same front skin absorption as the reference case (about 49% of E_{ini}). The back skin, however, absorbs less energy (22% of E_{ini} compared to 49% for A_{ref}). This is due to the fact that the core dissipates part of the energy absorbed by the rear skin in the plates alone. However, at 130 m/s, both skins absorb less energy than in skins alone and are perforated. This is due to the core presence, which tends to localize the stress in the skins, inducing their premature rupture. At 130 m/s, the energy absorbed respectively in the front and rear skin decreased up to 39% and 32%, probably because of the earlier onset of rupture.

In sandwich structures, the core absorbs part of the impact energy, which induces a proportional decrease of the energy dissipated in the rear skin. On the other hand, it localizes the stresses in the skin, due to the increasing of the peak and plateau values of the honeycomb under compression. This speeds up the moment of rupture of the front skin, which leads to the perforation of the sandwich. In principle, honeycomb shows good performances under impact, but when assembled in a sandwich structure, these performances are compromised due to these strong couplings between the core and the skins.

In conclusion, it can be mentioned that the results obtained from the numerical analysis were found to be in good agreement with the experimental results in terms of rupture prediction. The model predicts the initiation and localization of the rupture with a precision higher than ±8% in terms of impact velocity and kinetic energy. The sandwich model case B_1 is also tested and compared with the experimental results. It is found that the model has good accuracy in measuring projectile velocity evolution and rupture prediction. The sandwich model is then validated.

Conclusion

Experimental impact tests at 120 m/s have been conducted on several aluminium honeycomb sandwich targets, varying the velocity and target dimensions. A numerical analysis has been conducted using the finite element code ABAQUS/Explicit. Modified versions of the Johnson-Cook flow stress and rupture models have been implemented to represent the skins.

Numerical results underline significant strain rate effects in the honeycomb compression behavior. The numerical model does not predict the target rupture without considering these effects, while the experimentally associated cases are partially or totally perforated.

Therefore, a specific study on the dynamic compressive response of the honeycomb has been performed. A mesoscopic model has been defined to study the behavior of a single honeycomb cell at several compression velocities. The dynamical effects have been then implemented in the global sandwich model. Results obtained from the numerical analysis were found to be in reasonable agreement with the experimental results in terms of rupture prediction, and residual deformation profiles.

The behavior and performances of sandwich structures have been compared with the results of aluminium skins alone. The main aspects that can be drawn as a conclusion are:

1. The honeycomb core addition modifies the impact behavior in terms of resistance against perforation and maximal indentation. Regarding the first criterion, the core presence decreases the resistance under impact of the sandwich (as shown in Table 1 and Figure 5). Indeed, the skins–core interactions are significant as the core isolates the skins and the rupture occurs separately and earlier than in skins alone. However, the core addition increases the target flexural stiffness and decreases the maximum indentation ($+30\%$ back deflection in the plates alone).
2. The compression velocity has great influence on the compression behavior of honeycomb (ratio of 3 for the peak and plateau stresses between the quasi-static loading and 120 m/s). These dynamic effects in honeycomb decrease the sandwich performances. By localizing the stress in the front skin, they bring forward the rupture of the front skin, and thus the target perforation. These mechanisms provide new prospects related to the core properties and optimization. They suggest that the sandwich impact performance may be improved by the use of honeycombs without strain-rate dependencies or with low peak and plateau stresses.

Funding

The authors wish to thank the National Research Agency for the financial support through
6 the MANSART Project based on sandwich architectured materials. This work was granted
access to the HPC resources of CALMIP under the allocation 2010-P1026.

References

1. Dharmasena KP, Wadley HNG, Xue Z, et al. Mechanical response of metallic honeycomb sandwich panel structures to high-intensity dynamic loading. *Int J Impact Eng* 2008; 35: 1063–1074.
2. Rathbun HJ, Radford DD, Xue Z, et al. Performance of metallic honeycomb-core sandwich beams under shock loading. *Int J Solids Struct* 2006; 43: 1746–1763.
3. D'Angelo MM, Gallman J, Johnson V, et al. *Small commercial efficient & quiet air transportation for year 2030–2035*. Technical Report NASA/CR-2010-216691, 2010. ▮: ▮. 7
4. Abdulhamid H, Kolopp A, Bouvet C, et al. Experimental and numerical study of AA5086-H111 aluminium plates subjected to impact. *Int J Impact Eng* 2012; 51: 1–12.
5. Goldsmith W, Wang G, Li K, et al. Perforation of cellular sandwich plates. *Int J Impact Eng* 1997; 19: 361–379.
6. Buitrago BL, Santiuste C, Sánchez-Sáez S, et al. Modeling of composite sandwich structures with honeycomb core subjected to high-velocity impact. *Compos Struct* 2010; 92: 2090–2096.
7. Abrate S. Localized impact on sandwich structures with laminated facings. *Appl Mech Rev* 1997; 50: 69–82.

8. Castanie B, Bouvet C, Aminanda Y, et al. Modelling of low-energy/low-velocity impact on Nomex honeycomb sandwich structures with metallic skins. *Int J Impact Eng* 2008; 35: 620–634.
9. Aminanda Y. *Contribution à l'analyse et à la modélisation de structures sandwiches impactées*. Thèse de doctorat, [redacted], 2004. 8
10. Asadi M, Shirvani H, Sanaei E, et al. A simplified model to simulate crash behavior of honeycomb. In: *Proceedings of the international conference of advanced design and manufacture*, Harbin, China, [redacted] 2006. 9
11. Klinworth J and Stronge W. Elasto-plastic yield limits and deformation laws for transversly crushed honeycombs. *Int J Mech Sci* 1988; 30: 273–292.
12. Zhao H, Elnasri I and Abdennadher S. An experimental study on the behavior under impact loading of metallic cellular materials. *Int J Mech Sci* 2005; 47: 757–774.
13. Radford DD, McShane GJ, Deshpande VS, et al. Dynamic compressive response of stainless-steel square honeycombs. *J Appl Mech* 2007; 14: 658–667.
14. Elnasri I. *Comportement de matériaux cellulaires sous impact et de panneaux sandwiches sous perforation dynamique*. Thèse de doctorat, [redacted], 2007. 10
15. Levy N and Goldsmith W. Normal impact and perforation of thin plates resulting from projectile impact. *Int J Impact Eng* 1984; 2: 299–324.
16. Hou B, Ono A, Abdennadher S, et al. Impact behavior of honeycombs under combined shear-compression. Part I: experiments. *Int J Solids Struct* 2011; 48: 687–697.
17. HexWeb^{TM}. Honeycomb attributes and properties. Data sheet. 11
18. Evans AG, Hutchinson JW and Ashby MF. Cellular metals. *Solid State Mater Sci* 1998; 3: 288–303.
19. Gibson LJ and Ahsby MF. *Cellular solids: structure and properties*, 2nd ed. Cambridge: Cambridge University Press, 1997.
20. GuoWG, Zhang XQ, Su J, et al. The characteristics of plastic flow and a physically-based model for 3003 Al-Mn alloy upon a wide range of strain rates and temperatures. *Eur J Mech A-Solid* 2011; 30: 54–62.
21. Fleck NA and Hutchinson JW. A phenomenological theory for strain gradient effects in plasticity. *J Mech Phys Solids* 1993; 41: 1825–1857.
22. Begley MR and Hutchinson JW. The mechanics of size-dependant indentation. *J Mech Phys Solids* 1998; 46: 2049–2068.
23. Gao H. *Strain gradient plasticity, encyclopedia of materials: science and technology*. California: Stanford University, 2001, pp.8861–8865.